SCIENTIFIC REPORTS

OPEN

SUBJECT AREAS:
TERAHERTZ OPTICS
SUB-WAVELENGTH OPTICS
NANOPHOTONICS AND PLASMONICS
MICRORESONATORS

Received
10 December 2012

Accepted
14 February 2013

Published
1 March 2013

Correspondence and requests for materials should be addressed to Y.T. (yanko.todorov@univ-paris-diderot.fr)

Strong near field enhancement in THz nano-antenna arrays

Cheryl Feuillet-Palma, Yanko Todorov, Angela Vasanelli & Carlo Sirtori

Université Paris Diderot, Sorbonne Paris Cité, Laboratoire ''Matériaux et Phénomènes Quantiques'', CNRS-UMR 7162, FR-75013 Paris, France.

A key issue in modern photonics is the ability to concentrate light into very small volumes, thus enhancing its interaction with quantum objects of sizes much smaller than the wavelength. In the microwave domain, for many years this task has been successfully performed by antennas, built from metals that can be considered almost perfect at these frequencies. Antenna-like concepts have been recently extended into the THz and up to the visible, however metal losses increase and limit their performances. In this work we experimentally study the light coupling properties of dense arrays of subwavelength THz antenna microcavities. We demonstrate that the combination of array layout with subwavelength electromagnetic confinement allows for 10^4-fold enhancement of the electromagnetic energy density inside the cavities, despite the low quality factor of a single element. This effect is quantitatively described by an analytical model that can be applied for the optimization of any nanoantenna array.

Receiving antennas are devices that harvest the energy of free propagating electromagnetic waves and convert it into an AC voltage[1]. Antennas are widely used in the low frequency part of the electromagnetic spectrum, but recently nano-antenna devices have been explored up to the visible range[2–4]. Another way to apprehend the antenna operation is in terms of electric field, rather than voltage[5,6]. In this case, antennas can be seen as devices that are able to localize an oscillating electric field into a region of the space that is much smaller than the wavelength of light. Antennas are therefore closely related to microcavities, which also have the peculiar property to squeeze the electromagnetic energy into small volumes, for a particular resonant wavelength[6,7]. This property of antennas or mirocavities is now intensively investigated to extract and control the emission from single nano-scale objects such as molecules or quantum boxes[3,4,8,9].

The ability of some photonic structures to operate both as antennas and microcavities is best illustrated in the THz and micro-wave frequency regions, where metals are commonly used to confine light[1,10]. In this case the charges induced in the metal walls by an incident radiation can be clearly linked to the oscillating electric field in the resonator. Probably the best example is provided by the patch antenna, which consists of a metal ground, dielectric layer and a square patch of size s[1]. If the dielectric layer thickness L is much smaller than the wavelength, such structures support a TM_{100} mode with a frequency $\nu_0 = c/(2sn_{\mathrm{eff}})$, with c the speed of light and n_{eff} the effective index of the resonator. These cavities have been exploited to study the light-matter interaction in the THz and Mid-Infrared regions[11–13], and are widely used as antennas in the micro-wave region[1]. Antennas are now used also as a tool to optimize and control light extraction from Quantum Cascade Lasers operating in double-metal waveguides[14–16]. In this respect, the THz domain is also a formidable illustration of the crossover between optics and electronics. At sub-THz and microwave frequencies, patch antennas are used to capture an impinging electromagnetic radiation in order to feed oscillating electronic circuits. For frequencies above a few THz, these structures are used to concentrate light into a semiconductor region, enabling the radiation to excite oscillating microscopic dipoles originating from the electronic levels of nanometric-scale quantum heterostructures[11–13].

In the THz region and up to the Mid-Infrared, a very interesting property of these metallic structures is their strong sub-wavelength effective volume V[7] that boosts the light-matter interaction between the resonant mode and the electronic quantum transition[11,13]. The metallic patch antennas are well suited for these studies, as the electric field that they concentrate is perfectly aligned with the oscillating microscopic (intersubband) dipoles[11,13]. In this context, we recently demonstrated wire-shaped double-metal resonators, where the lateral dimensions of the patch have been reduced to highly sub-wavelength dimensions[17]. Funneling the incoming light into such small volumes can indeed be very useful for building very small active surface detectors with extremely low dark current. However, when reducing the resonator volume, a crucial question to be answered is how much of the incident energy is actually coupled inside the structure. Commonly, when an optical resonator is fed by an incoming wave, the energy density coupled inside the resonator is enhanced by an amount that is equal to the

resonator quality factor Q[18]. However, the strong squeezing of the electromagnetic field between metal layers always results in an increase of the ohmic losses and therefore it is important to understand the effects of higher losses on the near field enhancement of the device.

In this work we present an analytical approach that gives quantitative information on the properties of these plasmonic structures. The theoretical model is based on the fact that these double-metal structures act both as antennas and micro-resonators and is in full agreement with our experimental data, obtained by systematic studies of arrays of different geometry and filling factors. We will show that, both the arrangement of such antennas into periodic (but still sub-wavelength) array and the strong reduction of the resonator size allow a very efficient funneling of the incoming electromagnetic energy into very small volumes. Our results indicate up to 10^4 buildup of the electromagnetic energy density inside the resonant structures, despite their low quality factors $Q \sim 60$. Moreover, the main results from this model are expressed in a form that is free from the details of our experimental system. We therefore believe that the concepts developed in this work can be very useful for the optimization of any antenna-coupled resonant photonic structure.

Results

Reflectivity measurements on wire microcavities. The structure studied in this work is depicted in Figure 1. Fig. 1(a) is a schematics of a single wire microcavity, Fig. 1(b) is a top view of a portion of the array, obtained by scanning electron microscope (SEM), and Fig. 1(c) is high resolution SEM scan along the red rectangle in Fig. 1(b). This structure is obtained by Au-Au bonding of a thin Gallium Arsenide (GaAs) layer on a host substrate. The gold bonding layer then plays the role of the metallic ground of the microcavity. An array of thin Au stripes is then deposited on the top of the GaAs layer. The microcavity operates on the fundamental TM_{100} mode, with a resonant wavelength $\lambda_{res} = 2n_{eff}s$, with s the length of the stripe, and $n_{eff} \sim 4$ the effective index[17]. For all structures reported here $s = 12$ μm, therefore the resonant frequencies span between 3 THz and 4 THz (Fig. 2), which corresponds to a wavelength range $\lambda = 75$ μm–100 μm. Both the width w of the stripe and the thickness L of the GaAs layer have very subwavelength dimensions. Two different thicknesses have been used in our experiments, $L = 1$ μm and $L = 300$ nm, and for all structures we have $w = 1$ μm.

To probe the cavity resonances, we have performed reflectivity measurements under almost normal incidence, as described in Figure 2(a). The incident light was polarized along the cavity length (the x-direction, Fig. 1(a) and Fig. 2(a)), in order to respect the selection rule for the TM_{100} mode[19]. In Figs. 2(b) and 2(c), we report the reflectivity curves measured with two sets structures with $L = 1$ μm and $L = 300$ nm. The absolute reflectivity is obtained by dividing the spectra by a reference obtained with gold mirror and a baseline correction. The resonant cavity mode appears as a reflection dip in the spectra. In these experiments, we vary the lateral spacing d_y between the resonators (see Fig. 1(b,c) and Fig. 2(a)). The value of the longitudinal spacing d_x is kept constant, $d_x = 3$ μm. The grating periods are kept subwavelength, so that the only contribution in the reflected signal is the specular reflection (0^{th} diffraction order). In the plots of Fig. 2(b,c), the experimental data are represented by symbols, and the continuous lines are Lorentzian fits. For the experimental spectra, the crossed curves indicate measurements from a repeat sample with the same parameters as the one indicated in dots.

The measurements reported in Fig. 2(b) and (c) display two main features. The first is that the resonant frequency remains constant when the cavities are sufficiently apart, ($d_y \geq 3$ μm), while it is progressively red-shifted while the cavities are brought closer. This behavior arises from a near field coupling between the cavities that has been discussed elsewhere[17]. The second main feature of the experimental data is the progressive decrease of the amplitude of the dips (the dip contrast, C) as d_y is increased and the density of the arrays is reduced. That means that the ability of the structure to absorb and dissipate photons is altered by the geometry of the array. These measurements therefore allow gaining a quantitative insight for the funneling of the incident electromagnetic wave into the resonators.

Analysis of the experimental data. The experimental quantities that describe the ability of the structure to interact with the incoming radiation are the quality factor of the resonances Q and their

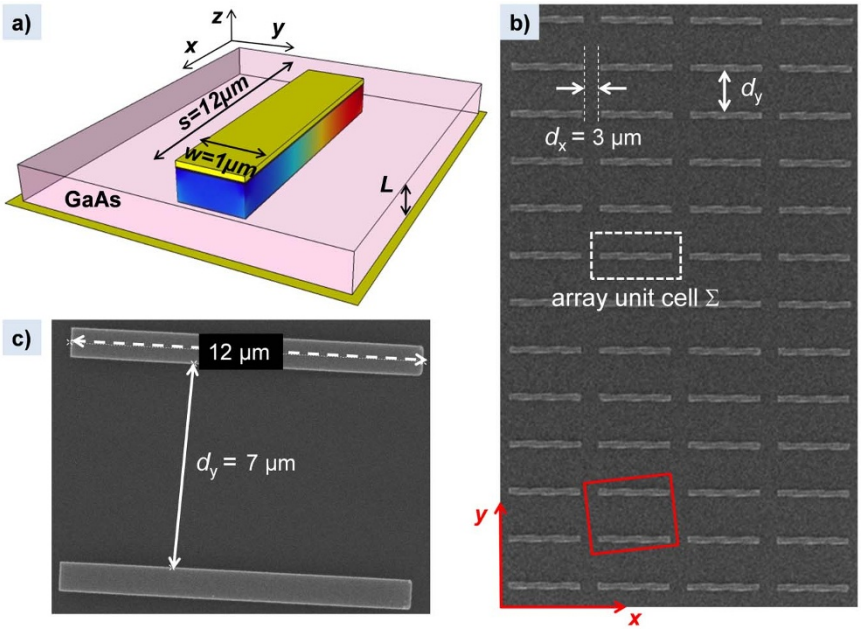

Figure 1 | Array of double metal wire resonators. (a) Schematics of a single wire micro-cavity. A GaAs layer of thickness L is sandwiched between a metal ground and a metal stripe with length s and width w. The colormap describes the fundamental TM_{100} mode of the structure. (b) SEM picture of an array of wire microcavities, indicating the relevant array dimensions. (c) High resolution SEM scan along the red rectangle indicated in (b).

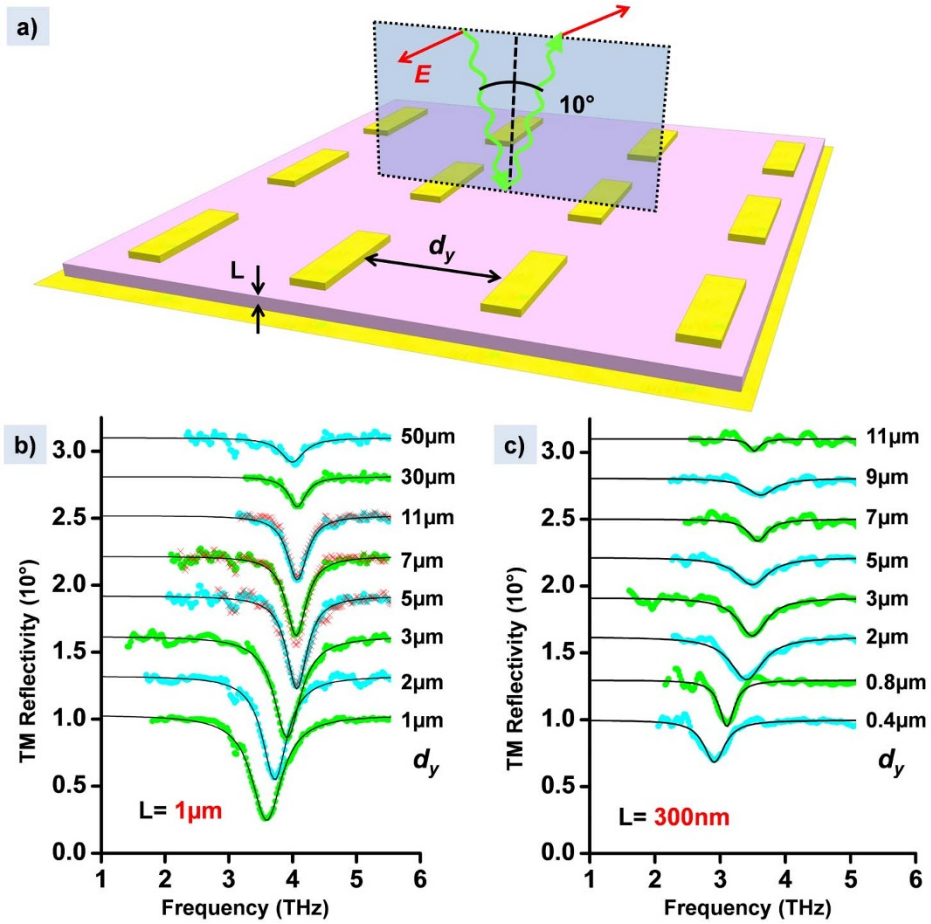

Figure 2 | Experimental characterization of the arrays. (a) Experimental configuration for reflectivity measurements performed at 10° incidence on arrays, with variable thickness L and lateral spacing d_y. The electric field E of the incident wave has also been indicated. (b,c) Reflectivity spectra obtained with thickness $L = 1$ μm (b) and $L = 300$ nm (c). The corresponding spacings d_y are indicated on the right. The experimental data is indicated by dotted curves, and the continuous lines are Lorentzian fits. The crossed curves indicate measurements from a repeat sample with the same parameters as the one indicated. The curves are shifted with a constant offset for clarity.

reflectivity contrast C, defined as $C = 1-R_{min}$, where R_{min} is the reflectivity minimum at the resonant frequency. Both these values can be extracted from the data through Lorentzian fits (continuous lines in Fig. 2(b) and (c)) of the form:

$$R(\nu) = 1 - \frac{C}{1 + \frac{(\nu-\nu_0)^2}{\pi^2\nu_0^2}Q^2} \qquad (1)$$

(In this work, the quality factors are defined as $Q = \omega_0/\Delta\nu = 2\pi\nu_0/\Delta\nu$, where $\Delta\nu$ is the FWHM of the reflectivity dip. Note that there is an additional 2π factor with respect to the definition used in Ref.19.) The contrast C is determined by the balance between the reflected photons and those absorbed by the array of resonators. The quality factor Q incorporates the radiation losses, $1/Q_{rad}$, and the ohmic losses of the metal layers, $1/Q_{ohm}$, through $1/Q = 1/Q_{rad} + 1/Q_{ohm}$. The error bars indicated in Fig. 3 are estimated from the repeat measurements reported in Figs. 2(b),(c), which provide a standard mean deviation of 0.06 for the contrast C and 10% of uncertainties for the quality factors Q.

Our main theoretical result is to provide a link between the absorption properties of the array to the radiation properties of a single antenna element. This link is contained into an explicit analytical relation between the reflectivity contrast C and the ratio Q_{rad}/Q_{ohm}. To derive this relation we have used the Poynting's theorem and matched the incoming plane wave to the fringing fields of the structure, seen as an antenna. As a corollary, we also obtain the ratio between the amplitudes of the incoming wave and the mode resonantly excited in the microcavity. The detailed derivation is presented in the Methods section. Here we provide the main theoretical results that can be directly compared with the experimental data. The expression for the contrast C for the case of normal incidence with x-polarized light (TM polarization) is:

$$C = \frac{4\alpha}{(1+\alpha)^2}, \quad \alpha = \frac{A_{eff}}{\Sigma}\frac{Q_{ohm}}{Q_{rad}} \qquad (2)$$

In this formula, Σ is the unit cell surface of the periodic array, that is in our case $\Sigma = (s + d_x)x(w + d_y)$. The quantity A_{eff} is the antenna effective area defined as: $A_{eff} = \lambda^2 \times (dP_{rad}/d\Omega)/P_{rad}$, whith P_{rad} the total radiated power and $dP_{rad}/d\Omega$ is the maximum radiated intensity[20]. The quantity α introduced in Eq.(2) can be seen as the ratio between the photon in-coupling rate ($1/Q_{rad}$) and the absorption rate ($1/Q_{ohm}$) corrected by the geometrical ratio A_{eff}/Σ. In this respect, the result of Eq.(2) is analogous to the theory describing the coupling between a waveguide and a resonator[21]. Indeed, a maximum contrast $C = 1$ is obtained when all the incident power flow is absorbed by the structure. This situation is known in optics as critical coupling regime[21]. In our case it is obtained when $\alpha = 1$, that is a perfect match between the power dissipated in the microcavity array and the power coupled inside the array.

In order to treat the experimental data, we calculate the quantities A_{eff} and Q_{rad} using microwave antenna theory[20]:

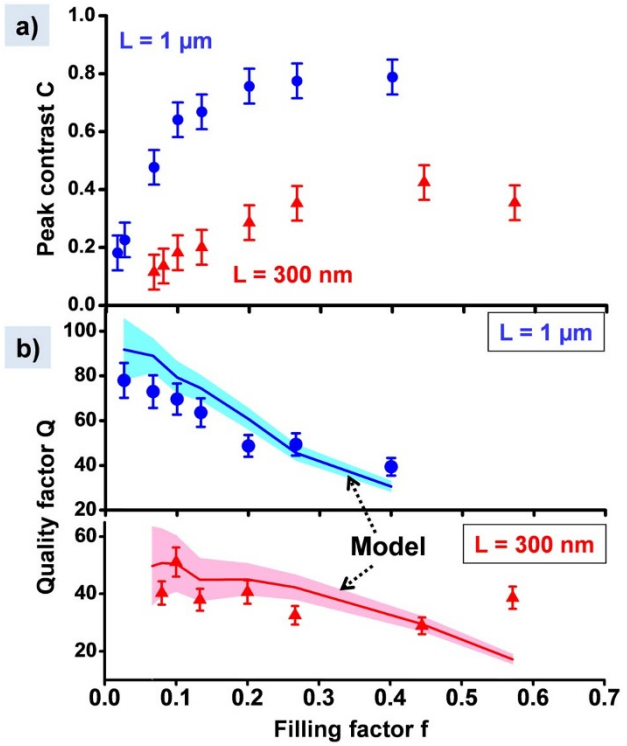

Figure 3 | Summary of the reflectivity measurements. (a) Contrast of the reflectivity resonances C as a function of the filling factor f for the gratings from data Figs. 2(b) and 2(c). (b) The respective quality factors Q (dotted curves), compared to the model (continuous curves). The shaded areas correspond to the standard mean deviations of the model, computed from the error bars of the contrast C and Eq.(2).

$$A_{eff} = \frac{\lambda^2}{3.2},\ Q_{rad} = \frac{\pi\varepsilon}{4n_{eff}}\frac{A_{eff}}{wL} \tag{3}$$

Here $\varepsilon = 12.2$ is the dielectric constant of the bulk GaAs. The model described in the Method section also allows deriving the ratio between the electromagnetic energy density circulating in each cavity and the energy density of the incoming wave:

$$\frac{\varepsilon|E_{z0}|^2}{|E_{in}|^2} = \frac{\lambda_{res}\Sigma}{2\pi V}Q_{ohm}C\cos\theta \tag{4}$$

Here $V = wLs$ is the volume of the resonator, E_{in} is the electric field amplitude of the incoming wave, E_{z0} is the amplitude of the mode resonantly excited in the microcavity, and θ is the angle between the incoming wave and the normal of the device. For the data reported here we have $cos\theta \sim 1$.

Our treatment of the experimental data is presented in Figure 3. In Fig. 3(a) we report the reflectivity contrast for the two sets of samples, extracted from the data presented in Fig. 2, as a function of the array filling factor f defined as $f = sw/\Sigma$. In Fig. 3(b) we present, as dotted curves, the quality factors Q of the resonances obtained directly from the Lorentzien fits through Eq.(1). According to Eq.(3), the typical values of Q_{rad} are $\sim 5.5 \times 10^3$ for $L = 1$ μm and $\sim 2 \times 10^4$ for $L = 300$ nm. These values are much higher than the values of Q observed In Fig. 3(b), we therefore conclude that, according to the relation $1/Q = 1/Q_{ohm} + 1/Q_{rad}$, the overall quality factor is essentially dominated by the ohmic loss of the microcavities, $Q \sim Q_{ohm}$. This means that the system is in the undercoupled regime, $\alpha < 1$, in agreement with previous studies on THz photonic crystal structures[22]. According to Eq.(2), another way to obtain Q_{ohm} is from the measurement of C reported in Fig. 3(a). Combining Eq.(2) and Eq.(3) we obtain $\alpha = fQ_{ohm}(4n_{eff}L/(s\pi\varepsilon))$, which, together with the condition $\alpha < 1$ allows to relate directly the contrast C to Q_{ohm}. The resulting values of Q_{ohm} are reported as continuous lines in Fig. 3(b). The shaded areas in Fig. 3(b) correspond to the standard mean deviation of the model, obtained from the error bars of C. The match is very good for both the $L = 1$ μm and $L = 300$ nm structures, within the experimental uncertainties. This proves the self-consistency of the model described by Eq. (2), which sets a correlation between the linewidths and amplitudes of the reflectivity dips in the experimental spectra.

Having validated our theoretical model through comparison with measurements, we can now provide quantitative estimation of the parameters relevant to the emission and absorption of radiation. These parameters are the light extraction efficiency defined as Q/Q_{rad}[1], and the ratio between the energy densities of the electromagnetic field inside the microcavity and that of the incoming field (Eq.(4)). They are plotted respectively in Figures 4(a) and 4(b).

Not surprisingly, the extraction efficiency is strongly hindered for the smaller thickness $L = 300$ nm. Part of this tendency is explained by the formula for the radiative quality factor Q_{rad}, which increases as $1/L$. However, the strong squeeze of the electric field between the metal plates separated by L also increases the ohmic loss, thus further reducing Q_{ohm}. This is also clear from the data in Fig. 3(b), since the ohmic loss is the dominant contribution in Q. Interestingly, for both thicknesses, the extraction efficiency decreases for high filling factors f. This behavior indicates an increase of the losses as the array

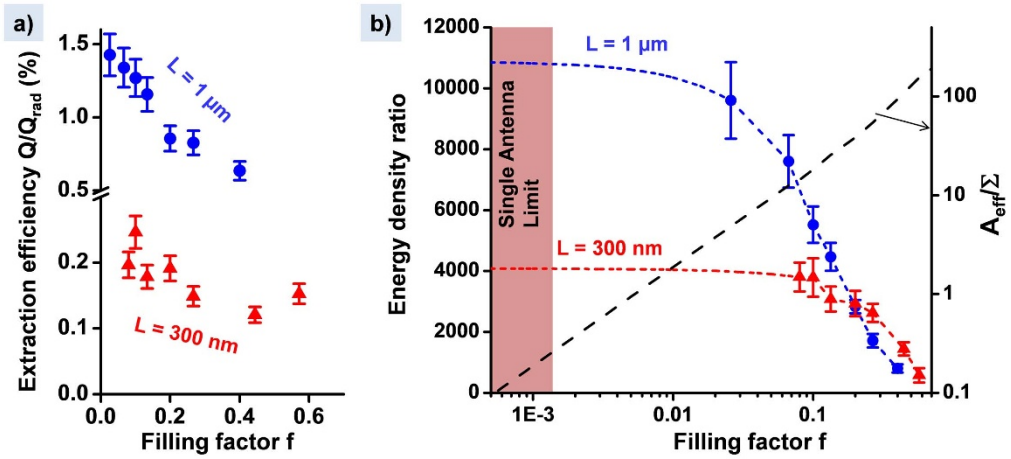

Figure 4 | Analysis of the reflectivity data. (a) The light extraction efficiencies of the samples, defined as the ratio Q/Q_{rad}. (b) Ratio between the electromagnetic energy densities of the microcavity field and the field of the incoming plane wave. The short-dashed lines are extrapolation of the data for vanishing filling factors. The long-dashed line indicates the ratio A_{eff}/Σ (right axis). The shaded area corresponds to the single antenna limit, $A_{eff}/\Sigma \leq 1$. In both (a) and (b) the error bars are estimated from those of C and Q reported in Fig. 3.

becomes denser, and can be related to near field phenomena that appear for small grating periods[19], such as light funneling mechanisms[23]. Indeed, as previously reported, for dense arrays the losses are enhanced by the grating evanescent waves propagating along the array[19].

Similar trend is observed for the energy density ratio, as seen from the plot in Figure 4(b). For low filling factors, very high ratios are observed, resulting in strong enhancement of the energy density of the microcavities: $\sim 10^4$ for the $L = 1$ μm array, and $\sim 4 \times 10^3$ for the $L = 0.3$ μm array. Similar enhancement factors have been theoretically predicted with bow-tie THz antennas[24]. Note that this factors are several orders of magnitude higher than the resonators quality factors ($Q \sim 60$), that also set the limit for the maximum enhancement in the naïve single resonator picture. Such strong enhancement is due to the presence of the factor $\lambda_{res}\Sigma/V \sim n_{eff}\Sigma/wL$ in Eq.(4), and is a direct consequence of the reduction of the transverse resonator dimensions into highly sub-wavelength values.

As for the case of the extraction efficiency, the energy density enhancement (Eq.(4)) decreases in the limit of high filing factors $f \to 1$ because of strong decrease Q_{ohm}. However, we observe a crossover between the $L = 1$ μm structures and the $L = 300$ nm structures at $f = 0.2$. Indeed, for high values of the array filling factor ($f > 0.2$) the enhancement for the $L = 300$ nm structures is slightly higher than that of the $L = 1$ μm structures in spite of the fact that the contrasts and quality factors are lower in that limit. This is because the contribution of the geometrical factor Σ/wL is higher for the smaller thickness. The combination of a strong subwavelength confinement with an array configuration is therefore very beneficial for concentrating the electromagnetic energy into small regions of space.

It is very interesting to examine the near field enhancement that can be obtained in the limit of very low filling factors, where $f \to 0$ and $\Sigma \to \infty$. This limit can be obtained when $d_y \to \infty$. Since at some point the array period $w + d_y$ will become comparable and greater than the resonant wavelength, we must take into account the high order diffracted waves. However, as explained in the Method section, as long as the gap d_x is kept very sub-wavelength ($d_x \ll \lambda$), and for normal incidence ($\theta \sim 0$), the diffraction does not intervene and all the results Eq. (2)–(4) remain valid. In this case we can estimate from Eq.(2) that the contrast C decreases as $C \to (4A_{eff}/\Sigma)(Q_{ohm}/Q_{rad})$. Replacing in Eq.(4), we find an asymptotic value of the enhancement parameter:

$$\left.\frac{\varepsilon|E_{z0}|^2}{|E_{in}|^2}\right|_{f\to 0} \to \frac{2\lambda_{res}A_{eff}}{\pi V}\frac{Q_{ohm}^2}{Q_{rad}} \qquad (5)$$

It is apparent that this limit depends only on the parameters of a single receiving element. In our case, in which we deal with patch antenna, the limit has a very simple form as the volume of the antenna and the volume of the microcavity are in our case equal and cancel out:

$$\left.\frac{\varepsilon|E_{z0}|^2}{|E_{in}|^2}\right|_{f\to 0} \to \frac{16}{\varepsilon\pi^2}n_{eff}^2Q_{ohm}^2 \qquad (6)$$

In the case patch antennas, therefore, the limiting value (6) depends only on the square of the resonator quality factor. The extrapolation of the data for very small filling factors is plotted as dashed lines in Fig. 4(b), showing the saturation of the enhancement at the limiting value of Eq. (6). On the same graph, we have also plotted the ratio A_{eff}/Σ between the antenna effective area and the grating unit cell. The saturation is clearly attained when $A_{eff} < \Sigma$, where the behavior of the system is dominated by that of a single antenna.

Beyond the case of patch-antennas, in general the micro-resonator and the antenna can be different objects, and the confinement volume will not necessarily cancel out. Then Eq.(5) clearly indicated how the combination between antennas with high radiation loss with a very small volume microcavity can lead to an important enhancement of the electromagnetic field inside the cavity.

Discussion

Our results set general relationships between the electromagnetic power dissipated in a nano-antenna array, the electromagnetic energy density enhancement and the geometrical characteristics of the system, such as the array filling factor. Depending on the particular applications, the analytical results described in Eq.(2)–(5) can be used to optimize a given device.

Consider, for instance, the case where the semi-conductor layer is filled with photoconductive media, such as doped shallow quantum wells as in a typical Quantum Well Infrared Photodetector (QWIP) device[25]. Another possible example is the micro-bolometer detectors relying on planar antennas[26]. In this case an important quantity is the contrast C which describes how much of the incident power is coupled inside the detector active medium. The latter, however, is partially dissipated by the metal losses and does not contribute to the photocurrent signal. For the detector the total non-radiative loss is then described by a quality factor $1/Q_{nr} = 1/Q_{ph} + 1/Q_{ohm}$ which takes into account both contributions, from the metal $1/Q_{ohm}$ and from the photoconductive media, $1/Q_{ph}$. In this case we should use Q_{nr} instead of Q_{ohm} everywhere in Eq.(2)–(6). The figure of merit of the system is therefore CxQ_{nr}/Q_{ph} which is also directly proportional to the detector responsivity. If the photoconductive loss is small, $1/Q_{ph} \ll 1/Q_{ohm}$ this figure of merit becomes CxQ_{ohm}/Q_{ph} with C independent from Q_{ph}. In this case the optimal responsivity of the detector can be evaluated using the values of C and Q reported in Figure 3(a,b). The result is plotted in Figure 5(a) which provides an optimum filling factor for a detector array of a given thickness. When $1/Q_{ph}$ cannot be neglected with respect to $1/Q_{ohm}$, Eq.(2) provides a

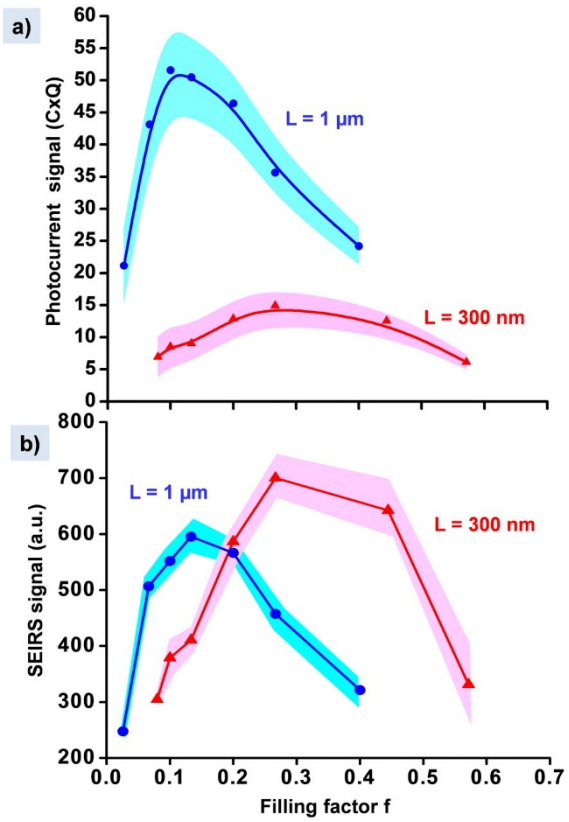

Figure 5 | Possible array optimizations. (a) A figure of merit of a possible detector device build with our THz nano-antenna array. (b) Optimization of the array from the point of view of a SEIRS experiment. The shaded areas correspond to the standard mean deviation of the model.

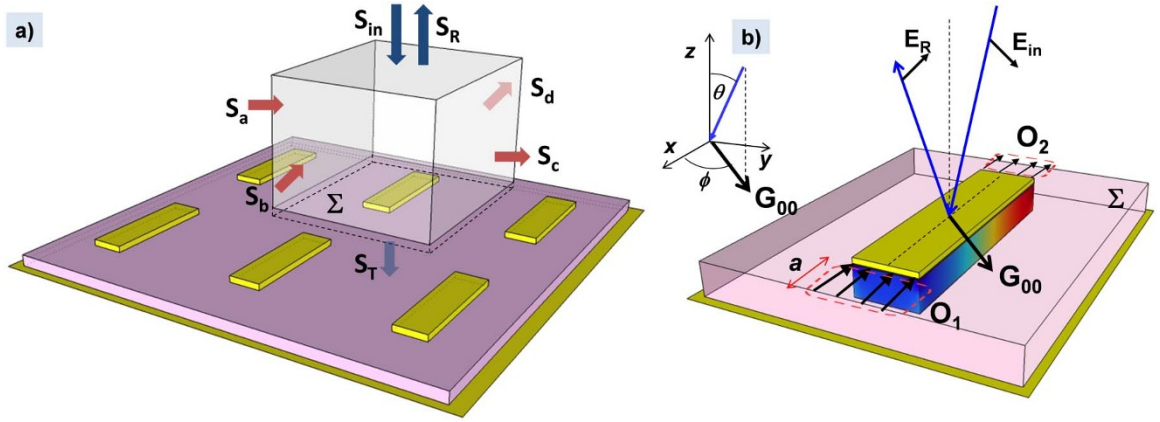

Figure 6 | Geometrical layout for our model. (a) Schematic of the volume used to express the energy flow conservation in our system. The volume lays on a unit cell of the array. The different Poynting fluxes normal to the surfaces are indicated. (b) Representation of the incoming electric field projection and of the fringing fields for a single resonator. The inset indicates the polar angles describing the direction of the incident plane wave. The parameter *a* is the typical extension of the fringing fields.

relationship between the contrast C and Q_{nr}, and the optimization can still be performed.

Another example of interest are the surface enhanced infrared spectroscopy (SEIRS) or surface enhanced Raman scattering spectroscopy (SERS) which rely on metallic nano-particle arrays[27]. In this case each nano-particle acts as an antenna in order to provide a local field enhancement and increase the detection sensitivity[28]. For these techniques the overall response is proportional to $\varepsilon\,|E_{0z}|^2/|E_{in}|^2$ (for a SERS signal we should rather consider $\varepsilon^2|E_{0z}|^4/|E_{in}|^4$) multiplied by the number of cavities illuminated by an incident beam with a spot size S_{beam}. The number of cavities illuminated is $S_{beam}/\Sigma = S_{beam}/ws \times f$ and therefore proportional to the filling factor. Once again, our results in Eq.(4–6) indicate clearly how such optimization can be performed. The figure of merit for SEIRS becomes $f \times \varepsilon\,|E_{0z}|^2/|E_{in}|^2$ and has been plotted in Fig. 5(b), showing that thinner structures could have better performance for higher filling factors. Remarkably, this trend is opposite as compared to the case of detectors (Fig. 5(a)), that are optimized for lower filling factors and a larger thickness. More generally, for a given micro-antenna array, our model predicts a maximum overall signal collected from a SEIRS or a photodetection experiment as a function of the geometry of the system.

These examples show how the combination between metallic resonant structures providing strong near field enhancement and a two-dimensional patterning add degrees of freedom to the optimization of a number of devices, which go beyond the context of the experiments described in this paper. Indeed, our theoretical treatment is based on general concepts like energy conservation and antenna theory. Therefore this approach can be adapted to any type of periodic array and any antenna geometry. Indeed, the final results stated in Eq.(2) and Eq.(4) have a very general form, independent from the particular type of antennas. We therefore believe that they have wider domain of application, and can be used to describe, for instance, light absorption from meta-material arrays[29] or nano-antennas in the visible[3]. In particular, our results describe quantitatively the near field enhancement in systems such as very small volume microcavities combined with high radiation loss antennas. Note that our studies do not rely on concepts like phase arrays[20] which basically exploit the constructive interference of light emitted or transmitted from each element[30]. This is because our results were established for the case where the high diffraction orders can be neglected.

The concepts developed here could have an important impact for conceiving and realizing new plasmonic detectors of radiation. Actually, our results indicate how the electric field amplitudes in each absorbing element of the array can be enhanced, while the size of semiconductor active region can be greatly reduced. These structures can therefore allow increasing the ratio between the photocurrent (that is proportional to the electromagnetic energy density coupled in the structure) on the dark current of the detector.

Methods

Here we provide the detailed derivations of Eq.(2) and Eq.(4). The geometry of the model is described in Figure 6. We consider a TM polarized plane wave incident on the array, with an in-plane wavevector $\mathbf{G}_{00}$ with components:

$$G_{00x} = \frac{2\pi}{\lambda}\sin\theta\cos\phi,\ \mathbf{G}_{00y} = \frac{2\pi}{\lambda}\sin\theta\sin\phi \tag{7}$$

Here θ and ϕ are the polar angles that correspond to the direction of the incoming wave with respect to the resonator axis as defined in Fig. 6. Moreover, we suppose that the field in the resonator is described by the standing wave equation $E_z = E_{z0}\cos(x\pi/s)$[19].

The first step to establish the result (2) is a very general energy conservation argument. Let us consider the Poynting's theorem[31] applied to the rectangular volume described in Fig. 6(a). The basis of the volume is the unit cell of the grating with a surface Σ. (Note that for an arbitrary array the volume is rhomboidal which does not change the final result.). According to the periodicity of the system, for this particular choice the Poynting fluxes incoming to a pair of opposite lateral surfaces are exactly equal, $S_a = S_c$ and $S_b = S_d$. However, their contribution to the energy variation of the volume has an opposite sign with respect to the normal of the surfaces, and therefore they cancel out. Therefore the energy conservation must account only for the upper and the lower surface of volume and takes a very simple form:

$$\Sigma(S_R - S_{in}) = \Sigma S_T + \iiint_V \mathbf{j}\mathbf{E}d^3\mathbf{r} \tag{8}$$

Here S_{in} and S_R are the z-components of the incoming and the reflected Poynting fluxes, averaged over the unit cell of the grating, S_T is the Poynting flux through the metal ground and the last term describes the ohmic losses in the metal stripe and eventually in the semiconductor region of the resonator. Since the metal ground is optically thick, no field tunnels through, and the flux S_T is all lost as ohmic dissipation. The right hand side of Eq.(8) describes therefore all the non-radiative loss of the resonator. We can define a non-radiative quality factor Q_{ohm} through the relation:

$$\left.\frac{dU}{dt}\right|_{nr} = \frac{\omega_0 U_0}{Q_{ohm}} = \Sigma S_T + \iiint_V \mathbf{j}\mathbf{E}d^3\mathbf{r} \tag{9}$$

Here $\omega_0 = 2\pi\nu_0$ and we introduced the total electromagnetic energy stored in the resonator: $U_0 = \varepsilon\varepsilon_0|E_{z0}|^2 swL$, by neglecting the contribution of the fringing fields[17]. To further explicit relation (8), we use the Rayleigh-Bloch decomposition[32] of the field in the air that can be expressed in terms of the incoming and reflected electric fields:

$$E_z = \sum_{\mathbf{G}} |\mathbf{G}| e^{i\mathbf{G}\mathbf{r}}(\delta_{\mathbf{G},\mathbf{G}_{00}} e^{i\gamma_{\mathbf{G}}z} + R_{\mathbf{G}} e^{-i\gamma_{\mathbf{G}}z}),\ \gamma_{\mathbf{G}}^2 = k_0^2 - \mathbf{G}^2 \tag{10}$$

$$\mathbf{E}_{//} = -\sum_{\mathbf{G}} \frac{\mathbf{G}\gamma_{\mathbf{G}}}{|\mathbf{G}|} e^{i\mathbf{G}\mathbf{r}}(\delta_{\mathbf{G},\mathbf{G}_{00}} e^{i\gamma_{\mathbf{G}}z} - R_{\mathbf{G}} e^{-i\gamma_{\mathbf{G}}z}) \tag{11}$$

Here $\mathbf{G} = \mathbf{G_{00}} + \mathbf{G}'$ with $\mathbf{G}'$ the reciprocal lattice vectors, $\mathbf{r} = (x,y)$ is the in-plane position vector, c is the speed of light, $k_0 = \omega_0/c$ and $E_{//} = E_x, E_y$ are the horizontal electric field components. The expressions for the magnetic field components H_y and H_x can be easily derived from Maxwell equations. The decomposition (10) contains a

set of reflected waves with amplitudes R_G, however, since our grating is very sub-wavelength ($\Sigma < \lambda^2$), only the 0^{th} order is a propagating wave with amplitude R_{00} and contributes to the reflected Poynting flux S_R. Using the explicit expression of the z-component of the Poynting flux, $S_z = \mathrm{Re}(E_x H_y^* - E_y H_x^*)$, we rewrite (9) in the following form:

$$1-|R_{00}|^2 = \varepsilon \frac{swL}{Q_{ohm}} \frac{|E_{z0}|^2}{\Sigma \gamma_{00}} \tag{12}$$

This equation leads directly to Eq. (4). Indeed, the normalization of incident electric field corresponding to Eqs. (10,11) is $|E_{in}|^2 = k_0^2$, and the contrast is defined as $C = 1-|R_{00}|^2$. Furthermore, in Eq.(4) normal incidence is considered ($\theta = 0$), where $\gamma_{00} = k_0$.

The next step is to relate the reflectivity to the radiation loss. For this purpose, we consider our structure as a patch antenna, and we use the antenna theory[20]. Following the treatment provided in Ref. 20, we can express the in-plane components of the fringing electric field around the resonator openings as a function of the perpendicular component, E_z:

$$E_x(x=0) = \frac{L}{a} E_z(x=0),\ E_x(x=s) = -\frac{L}{a} E_z(x=s) \tag{13}$$

Here a is the extension of the fringing fields, as illustrated in Fig. 6(b). We have considered only the x-components, since the contribution of the E_y components cancels out due to the symmetry of the mode[20]. Matching the expressions (13) with the Bloch-Rayleigh expansion in the air (10), and integrating over the unit cell of the grating, we obtain:

$$\iint_{O_1 \cup O_2} \mathbf{G}_{00}.\mathbf{E}_{//}\big|_- e^{-i\mathbf{G}_{00}\mathbf{r}} d^2\mathbf{r} = \iint_{\Sigma} \mathbf{G}_{00}.\mathbf{E}_{//}\big|_+ e^{-i\mathbf{G}_{00}\mathbf{r}} d^2\mathbf{r} \tag{14}$$

In the above expression, we use (11) for $\mathbf{E}_{//}|_+$ and (13) for $\mathbf{E}_{//}|_-$. Note that this equation expresses the conservation of the in-plane electric field averaged over the area of the fringing fields and the unit cell of the lattice, respectively. By carrying out the integration, we obtain the relation:

$$\gamma_{00}(1-R_{00})\Sigma = LE_{z0}\left[1+\exp(-iG_{00x}s)\right]\left[1-\exp(-iG_{00y}w)\right]\frac{G_{00x}}{|\mathbf{G}_{00}|G_{00y}} \tag{15}$$

By taking the modulus squared of this expression and using Eq.(7) we obtain:

$$\gamma_{00}^2|1-R_{00}|^2\Sigma^2 = 4w^2L^2|E_{z0}|^2|F(\mathbf{G}_{00})|^2\cos^2\phi \tag{16}$$

Here $F(\theta,\phi)$ is the aperture function of the patch antenna, describing its radiation pattern, which writes:

$$\begin{aligned} F(\mathbf{G}_{00}) = F(\theta,\phi) &= \cos\left(\frac{G_{00x}s}{2}\right)\mathrm{sinc}\left(\frac{G_{00y}w}{2}\right) \\ &= \cos\left(\frac{\pi s}{\lambda}\sin\theta\cos\phi\right)\mathrm{sinc}\left(\frac{\pi w}{\lambda}\sin\theta\sin\phi\right) \end{aligned} \tag{17}$$

The ratio between the expressions (12) and (16) allows one to obtain the following equation:

$$\frac{|1-R_{00}|^2}{1-|R_{00}|^2} = \frac{4wL}{\varepsilon s k_0 \Sigma} Q_{ohm} \frac{\cos^2\phi}{\cos\theta}|F(\theta,\phi)|^2 \tag{18}$$

This equation still contains the parameters specific to the patch antenna. In order to obtain more general expression that could eventually apply to any antenna, we re-express the above equations as a function of the antenna effective area, provided by:

$$A_{eff} = \frac{\lambda^2}{D_{rad}} \tag{19}$$

where D_{rad} is the dimensionless angular integral:

$$D_{rad} = \int_0^{\pi/2}\int_0^{2\pi} |F(\theta,\phi)|^2(\cos^2\phi + \cos^2\theta\sin^2\phi)\sin\theta\,\mathrm{d}\phi\,\mathrm{d}\theta \tag{20}$$

We also use the radiative quality factor Q_{rad} provided by Eq.(3) . This leads to the final result:

$$\frac{|1-R_{00}|^2}{1-|R_{00}|^2} = \alpha = \frac{A_{eff}}{\Sigma}\frac{Q_{ohm}}{Q_{rad}}\frac{\cos^2\phi}{\cos\theta}|F(\theta,\phi)|^2 \tag{21}$$

Eq. (2) is then recovered assuming that the reflected wave has the same phase as the incoming wave, so that $|1-R_{00}| = 1-|R_{00}|$. We have checked numerically that this is the case when the gratings are sub-wavelength. We then re-express $|R_{00}|$ with the contrast through $C = 1-|R_{00}|^2$. The prefactor $\cos^2\phi$ expresses the polarization selection rule for the wire shaped structure, since ϕ is the angle between the electric field of the incoming wave and the wire (Fig. 6(b)). In the experimental conditions considered in the previous section we have $\phi = 0$ and $\theta = 0$ which leads to Eq.(2).

Similar derivation can be applied to treat any patch antenna structures arranged in any periodic array. The final result will be identical to Eq.(2) or Eq.(21), expect for the function $\cos^2\phi\ |F(\theta,\phi)|^2/\cos\theta$ that must be adapted for the particular geometry of the resonator. For instance, in the case of the higher order TM_{K00} mode of the wire resonators, equation (21) still holds if we define:

$$F(\theta,\phi) = \mathrm{sinc}\left(\frac{G_{00y}w}{2}\right) \times \begin{cases} \cos(G_{00x}s/2),\ K \text{ odd} \\ \sin(G_{00x}s/2),\ K \text{ even} \end{cases} \tag{22}$$

We therefore recover selection rules that are similar to those of the square patch cavities[19], which state that the even K modes are not excited in normal incidence (in this case $\alpha = 0$ and $C = 0$). More generally, formula (21) expresses the fact that the reflectivity selection rules arise from the radiation pattern of a single antenna. Therefore the absorption properties of a sub-wavelength antenna array can be engineered by adjusting the radiation pattern of a single element.

To extend this treatment to the case where higher diffraction orders are present, we must add their contributions $-(\gamma_G/\gamma_{00})|R_G|^2$ to the left hand side of Eq.(12). The amplitudes of the diffraction orders are readily obtained from Eq.(13), by replacing $\boldsymbol{G}_{00}$ with $\boldsymbol{G}$, which leads to:

$$\gamma_{\mathbf{G}}^2|R_{\mathbf{G}}|^2\Sigma^2 = 4w^2L^2|E_{z0}|^2|F(\mathbf{G})|^2\cos^2\phi_{\mathbf{G}} \tag{23}$$

Here we have defined $\cos^2\phi_{\mathbf{G}} = G_x^2/\mathbf{G}^2$. In the case where $d_x \ll \lambda$, and for normal incidence we have $\boldsymbol{G} = (0, 2\pi N/(w+d_y))$ with N an integer. We therefore have $\cos^2\phi_{\mathbf{G}} = 0$ for the high order diffraction amplitudes, and their contributions vanish.

1. Balanis, C. A. *Antenna Theory* (John Wiley & Sons, 2005).
2. Farahani, J. N. *et al.* Bow-tie optical antenna probes for single-emitter scanning near-field optical microscopy. *Nanotechnology* **18**, 125506 (2007).
3. Curto, A. G. *et al.* Unidirectional emission of a quantum dot coupled to a nanoantenna. *Science* **329**, 930–933 (2010).
4. Taminiau, T. H., Stefani, F. D., Segerink, F. B. & van Hulst, N. F. Optical antennas direct single-molecule emission. *Nature Phot.* **2**, 234–237 (2008).
5. Engheta, N. Metamaterials circuits with light at nanoscales: optical nanocircuits inspired by metamaterials. *Science* **317**, 1698 (2007).
6. Greffet, J.-J., Laroche, M. & Marquier, F. Impedance of a nanoantenna and a single quantum emitter. *Phys. Rev. Lett.* **105**, 117701 (2010).
7. Maier, S. A. Plasmonic field enhancement and SERS in the effective mode volume picture. *Opt. Express* **14**, 1957–1964 (2006).
8. Russell, K. J., Liu, T.-L., Cui, S. & Hu, E. L. Large spontaneous emission enhancement in plasmonic nanocavities. *Nature Phot.* **6**, 459–462 (2012).
9. Noda, S., Fujita, M. & Asano, T. Spontaneous-emission control by photonic crystals and nanocavities. *Nature Photon.* **1**, 449–458 (2007).
10. Adams, M. J. *An Introduction to Optical Waveguides* (John Wiley & Sons, Chichester, 1981).
11. Todorov, Y. *et al.* Ultrastrong light-matter coupling regime with polariton dots. *Phys. Rev. Lett.* **105**, 196402 (2010).
12. Geiser, M. *et al.* Ultrastrong coupling regime and plasmon polaritons in parabolic semiconductor quantum wells. *Phys. Rev. Lett.* **108**, 106402 (2012).
13. Jouy, P. *et al.* Transition from strong to ultrastrong coupling regime in mid-infrared metal-dielectric-metal cavities. *Appl. Phys. Lett.* **98**, 231114 (2011).
14. Hon, P. W. C., Tavallaee, A. A., Chen, Q.-S., Williams, B. S. & Itoh, T. Radiation model for Terahertz transmission-line metamaterial quantum-cascade lasers. *IEEE Trans. THz Sci. Technol.* **2**, 323–332 (2012).
15. Orlova, E. E. *et al.* Antenna model for wire lasers. *Phys. Rev. Lett.* **96**, 173904 (2006).
16. Walther, C., Scalari, G., Amanti, M., Beck, M. & Faist, J. Microcavity laser oscillating in a circuit-based resonator. *Science* **327**, 1495–1497 (2010).
17. Feuillet-Palma, C. *et al.* Extremely sub-wavelength THz metal-dielectric wire microcavities. *Opt. Express* **20**, 29121–29130 (2012).
18. Rosencher, E., Vinter, B. & Piva, P. G. *Optoelectronics* (Cambridge University Press, 2002).
19. Todorov, Y. *et al.* Optical properties of metal-dielectric-metal microcavities in the THz frequency range. *Opt. Express* **18**, 13886–13907 (2010).
20. Orfanidis, S. J. *Electromagnetic Waves and Antennas*, http://www.ece.rutgers.edu/~orfanidi/ewa/, last access: 02/10/2013.
21. Cai, M., Painter, O. & Vahala, K. J. Observation of critical coupling in a fiber taper to a silica-microsphere whispering-gallery mode system. *Phys. Rev. Lett.* **85**, 74–77 (2000).
22. Bahriz, M., Crisafulli, O., Moreau, V., Colombelli, R. & Painter, O. Design of mid-IR and THz quantum cascade laser cavities with complete TM photonic bandgap. *Opt. Express* **15**, 5948–5965 (2007).
23. Pardo, F., Bouchon, P., Haïdar, R. & Pelouard, J.-L. Light funneling mechanism explained by magnetoelectric interference. *Phys. Rev. Lett.* **107**, 093902 (2011).
24. Giannini, V., Berrier, A., Maier, S. A., Sánchez-Gil, J. A. & Rivas, J. G. Scattering efficiency and near field enhancement of active semiconductor plasmonic antennas at Terahertz frequencies. *Opt. Express* **18**, 2797–2807 (2010).
25. Schneider, H. & Liu, H. C. *Quantum well Infrared Detectors* (Springer-Verlag, Heidelberg, 2007).
26. Gonzalez, F. J. & Boreman, G. D. Comparison of dipole, bowtie, spiral and log-periodic IR antennas. *Infrared Phys. Technol.* **46**, 418–428 (2005).
27. Le, F. *et al.* Metallic nanoparticle arrays: a common substrate for both surface-enhanced Raman scattering and surface-enhanced infrared absorption. *ASC Nano* **2**, 707–718 (2008).

28. Biagioni, P., Huang, J.-S. & Hecht, B. Nanoantennas for visible and infrared radiation. *Rep. Prog. Phys.* **75**, 024402 (2012).
29. Scalari, G. *et al*. Ultrastrong coupling of the cyclotron transition of a 2D electron gas to a THz metamaterial. *Science* **335**, 1323–1326 (2012).
30. Blanchard, R. *et al*. Modeling nanoscale v-shaped antennas for the design of optical phased arrays. *Phys. Rev. B* **85**, 155457 (2012).
31. Landau, L. & Lifchitz, E. *Electrodynamics of Continuous Media* (Mir, Moscow, 1969).
32. Petit, R. *Electromagnetic theory of gratings* (Springer-Verlag, Berlin, 1980).

Acknowledgments

We gratefully acknowledge support from the French National Research Agency in the frame of its Nanotechnology and Nanosystems program P2N, Project No. ANR-09-NANO-007 and financial support from the ERC grant "ADEQUATE". We acknowledge sample growth by Giorgio Biasiol from IOM CNR, Laboratorio TASC (Italy) and Lucia Sorba from NEST, Istituto Nanoscienze-CNR and Scuola Normale Superiore (Italy).

Author contributions

C.F.-P. fabricated the samples, performed experiments and contributed to the writing of the manuscript, Y.T. contributed to the interpretation of the experimental data (model) and wrote the manuscript,
A.V. contributed to the writing of the manuscript, C.S. contributed to the interpretation of the experimental data contributed to the writing of the manuscript.

Additional information

Competing financial interests: The authors declare no competing financial interests.

How to cite this article: Feuillet-Palma, C., Todorov, Y., Vasanelli, A. & Sirtori, C. Strong near field enhancement in THz nano-antenna arrays. *Sci. Rep.* **3**, 1361; DOI:10.1038/srep01361 (2013).